small methods
www.small-methods.com

# A Universal Fabrication Strategy for High-Resolution Perovskite-Based Photodetector Arrays

*Yegang Liang, Qiuchun Lu, Wenqiang Wu, Zhangsheng Xu, Hui Lu, Zeping He, Yizhi Zhu, Yang Yu, Xun Han,* and Caofeng Pan**

**Metal halide perovskite photodetector arrays have demonstrated great potential applications in the field of integrated systems, optical communications, and health monitoring. However, the fabrication of large-scale and high-resolution device is still challenging due to their incompatibility with the polar solvents. Here, a universal fabrication strategy that utilizes ultrathin encapsulation-assisted photolithography and etching to create high-resolution photodetectors array with vertical crossbar structure is reported. This approach yields a 48 × 48 photodetector array with a resolution of 317 ppi. The device shows good imaging capability with a high on/off ratio of $3.3 \times 10^5$ and long-term working stability over 12 h. Furthermore, this strategy can be applied to five different material systems, and is fully compatible with the existing photolithography and etching techniques, which are expected to have potential applications in the other high-density and solvent-sensitive devices array, including perovskite- or organic semiconductor-based memristor, light emitting diode displays, and transistors.**

## 1. Introduction

In recent years, metal halide perovskites have emerged as the new generation of optoelectronic materials owing to their superior optoelectronic properties and cost-effective fabrication process. Continuous perovskite thin films have been widely employed in solar cells,[1] LEDs,[2] photodetectors,[3] with notable improvements in device performance. For example, perovskite solar cells have achieved a certified power conversion efficiency (PCE) of up to 25.7% in lab,[4] which paves the way for their commercialization. Compared with the device based on the continuous film,[5] the perovskite array devices offer unique properties and exciting possibilities for large-scale integrated systems. Addressable photodetector arrays are expected to make significant progress for imaging systems,[6] due to the high on/off ratio, fast response, and low dark current.[7]

Owing to the soft nature of perovskite materials,[8] they were vulnerable to the polar solvents and high temperature to decomposition,[9] rendering them incompatible with traditional photolithography processes.[10] Currently, a common fabrication strategy of the perovskite photodetector array is to synthesize the perovskite materials in the final step of the fabrication procedures, thereby avoiding potential damage to materials. This approach is well fitted with the planar device architecture of the perovskite photodetectors, where the perovskite is formed on the pre-fabricated electrode array. However, these devices typically exhibit large pixel dimension and limited resolution due to the complex electrodes distribution. Therefore, the high-resolution perovskite photodetectors array is still highly demanded for large-scale integration systems.

The vertical crossbar structure distributes the top and bottom electrodes on two different planes, offering a high device

Y. Liang, Q. Lu, Y. Yu, C. Pan
Center on Nanoenergy Research
School of Physical Science and Technology Guangxi University
Nanning, Guangxi 530004, P. R. China
E-mail: cfpan@binn.cas.cn

Y. Liang, Q. Lu, Z. Xu, H. Lu, Z. He, Y. Zhu, Y. Yu, C. Pan
CAS Center for Excellence in Nanoscience
Beijing Key Laboratory of Micro-nano Energy and Sensor
Beijing Institute of Nanoenergy and Nanosystems
Chinese Academy of Sciences
Beijing 101400, P. R. China

W. Wu
Institute of Microscale Optoelectronics
Shenzhen University
Shenzhen 518060, P. R. China

Z. Xu, H. Lu, Z. He, C. Pan
School of Nanoscience and Technology
University of Chinese Academy of Sciences
Beijing 100049, P. R. China

Y. Zhu
College of Physics and Optoelectronic Engineering
Shenzhen University
Shenzhen 518060, P. R. China

X. Han
ZJU-Hangzhou Global Scientific and Technological Innovation Center
School of Micro-Nano Electronics
Zhejiang University
Hangzhou311200, P. R. China
E-mail: xunhan@zju.edu.cn

The ORCID identification number(s) for the author(s) of this article can be found under https://doi.org/10.1002/smtd.202300339

**DOI: 10.1002/smtd.202300339**

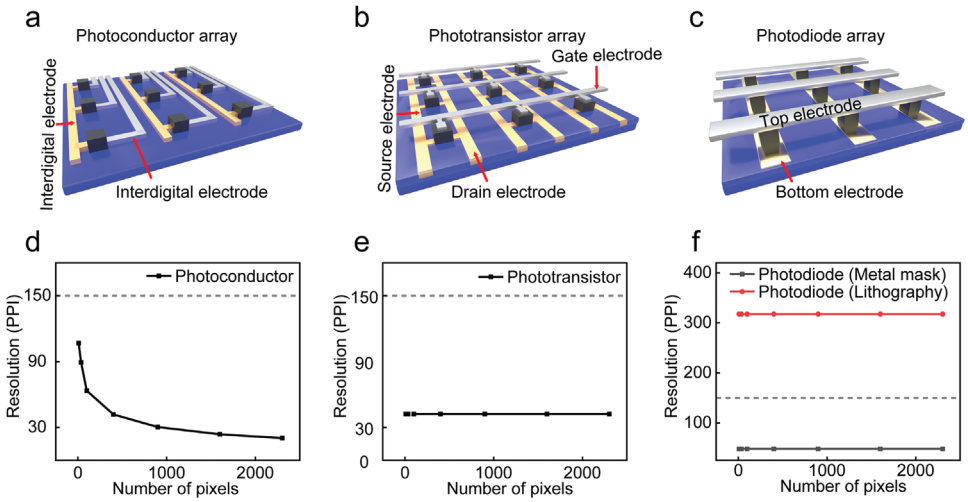


**Figure 1.** Three primary device structures for the perovskite photodetectors array. a–c) Schematic diagram of the structure of perovskite photoconductor, phototransistor, and photodiode array, respectively. d–f) Evolution of the resolution of the three device structures as pixel number increase, while remaining the width of circuit lines constant. The dotted lines in (d–f) are the reference lines.

integration density.[11] This structure can be readily adopted in the design of perovskite photodetectors array to improve its resolution. The crossbar perovskite array with photodiode-typed photodetector sandwiched by cross electrodes have been reported.[12] However, the top electrodes in these devices were fabricated through metal deposition with the shadow mask.[13] This may bring the misalignment between the pixels and top electrodes in the case of high pixel densities.[14] An ideal large-scale and high-resolution device should be compatible with the conventional microfabrication process, including photolithography and etching, to facilitate the integration with other functional or processing modules.

Here, we proposed a universal strategy for the high-resolution perovskite photodetector array. It adopts an ultrathin encapsulation layer to assist the top electrodes patterning, which enables the device fabrication process fully compatible with the photolithography and etching technologies. As the demonstration, we successfully fabricated a 48 × 48 self-powered perovskite photodetectors array with a resolution of 317 ppi. Each pixel consists a photodiode-typed photodetector with the structure of indium tin oxide (ITO)/nickel oxide ($NiO_x$)/$MAPbI_3$ (MA=$CH_3NH_3$)/fullerenes ($C_{60}$)/bathocuproine (BCP)/Ag. Due to the built-in electronic field, the device could work in the self-power mode, showing a high on/off ratio of $3.3 \times 10^5$, excellent sensitivity to weak light with an intensity of 5.4 nW $cm^{-2}$, and long-term operational stability for 12 h. Besides, benefiting from the uniform photoresponse from all the pixels, the high-resolution device can image the incident light distributions. More importantly, this strategy can be extended to different materials systems of the self-powered photodiode with various active layers, hole and electron transport layers (HTL and ETL). It bridges the gap between solvent-sensitivity materials and conventional microfabrication techniques, and is expected to facilitate the applications of high-resolution perovskite devices in the integrated optoelectronic systems.

## 2. Results and Discussion

### 2.1. Fabrication and Characterization of the Perovskite Array

Given the poor chemical stability of the perovskite materials, there are three primary device structures for the perovskite photodetectors array: perovskite photoconductors, phototransistors and photodiodes, as illustrated in **Figure 1**a–c. Perovskite photoconductors are typically fabricated by depositing perovskite films array on pre-patterned interdigital electrode arrays. In this structure, the electrode circuits are distributed between pixels, connected to form an integrated array (Figure 1a). For an array with m × n pixels, typically, m × n+1 terminals are required and at least half of the m or n circuits are laid out between adjacent pixels. Consequently, with increasing the pixel numbers, it takes considerable space between pixels to arrange the corresponding electrode circuits, which limits the resolution and scale of the perovskite photoconductor arrays (Figure 1d).[15] Perovskite phototransistors are similarly fabricated, but employ the hierarchical electrode circuits structure in which gate circuits are crossed with source or drain circuits and insulated with thin oxide films (Figure 1b). This design reduces the circuit space requirements, however, the maximum resolution is still limited by the fact that there are circuits distributed between the pixels (Figure 1e).[16] The photodiode configuration usually involves a vertical crossbar structure with column and row electrodes, as shown in Figure 1c. The electrodes are distributed above and below the pixel, respectively. Thus, the resolution does not change with increasing number of pixels (Figure 1f).[17] For the perovskite device, the fabrication of high density of top electrodes array is challenging as it involves the traditional photolithography process and polar solvents. Currently, the top electrodes are deposited using shadow masks, which could be difficult to align with the bottom high-resolution perovskite arrays, thereby, resulting to a resolution less than 100 ppi (black line in Figure 1f). Improving the density of

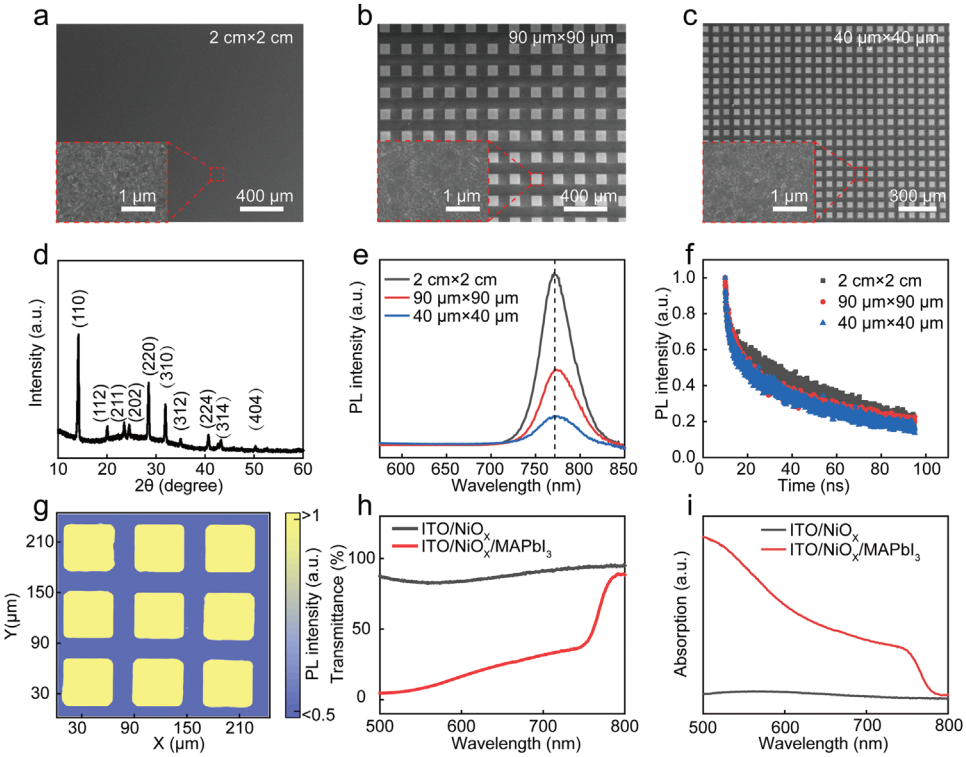


**Figure 2.** Characterization of the $MAPbI_3$ films array. SEM images of a) the continuous $MAPbI_3$ film with the area of 2 cm × 2 cm and the $MAPbI_3$ films array with pixel dimensions of b) 90 μm × 90 μm and c) 40 μm × 40 μm. The insets are the enlarged view of the perovskite film surface. d) XRD patterns of $MAPbI_3$ film. e,f) PL and TRPL spectrum of the continuous $MAPbI_3$ film with the area of 2 cm × 2 cm and the $MAPbI_3$ films array with pixel dimensions of 90 μm × 90 μm and 40 μm × 40 μm, respectively. g) The PL mapping spectrum of $MAPbI_3$ film array with pixel dimension of 40 μm × 40 μm. h,i) The transmission and absorption spectrum of ITO/HTL and ITO/HTL/$MAPbI_3$ films, respectively.

top electrode could enable the photodiode with vertical crossbar structure to achieve high resolution and large-scale devices, rendering it an ideal structure for perovskite photodetectors.

To increase the density of the top electrodes of the photodetector array, we proposed a fabrication strategy that utilizes the ultrathin encapsulation-assisted photolithography for patterning the electrodes. Figure S1 (Supporting Information) illustrates the fabrication steps of the high-resolution perovskite photodetectors array. Specifically, the bottom electrodes stripes were deposited on the substrate using photolithography to precisely define their positions. Then, a thin layer of SU-8 pattern was formed with its square openings aligned with the bottom electrodes stripes. This thin layer provides the confinement for the subsequent spin-coating process of the perovskite materials, while also functioning as an insulating layer between the top and bottom electrodes. Next, the HTL array was aligned with the SU-8 pattern, followed by the surface functionalization to generate hydrophobic areas. After spin-coating of the perovskite, the continuous ETL and metal layer were deposited and encapsulated by a thin layer of parylene film. The photoresist patterns with the same shape of the top electrodes were generated and dry etching was used to pattern the desired top electrodes, completing the fabrication process. The ultrathin encapsulation can protect the easily degradable HTL, ETL, and perovskite materials from the polar solvent, which enables the entire device fabrication process and photolithography compatible.

Achieving uniform performance of each pixel in the perovskite photodetectors array during pixel miniaturization process is crucial to its large-scale integration. To improve the uniformity of the perovskite film arrays, we adopted the SU-8 patterns to accurately define the pixel position, dimension and shape. The perovskite precursor solution was spin-coated onto the SU-8 patterns and confined in these patterns, followed by a controlled crystallization process to form the perovskite array. Two film arrays were fabricated, one with the pixel dimensions of 90 μm × 90 μm showing a resolution of 127 ppi, and the other with dimensions of 40 μm × 40 μm demonstrating an improved resolution of 317 ppi. As a comparison, a continuous film (2 cm × 2 cm) was achieved though spin-coating the precursor on a hydrophilic glass substrate. Scanning electron microscopy (SEM) images of the $MAPbI_3$ films of different dimensions are shown in **Figure 2**a–c. With the dimension decreasing, the morphology of the $MAPbI_3$ shows negligible changes, revealing a compact surface without pin holes and clear grain boundaries. The structure of the $MAPbI_3$ films was investigated by X-ray diffraction (XRD). As shown in Figure 2d, the diffraction peaks of $MAPbI_3$ films correspond to (110), (112), (211), (202), (220), (310), (312), (224), (314), and (404) lattice planes, representing the tetragonal $MAPbI_3$ structure.[18] In addition, the $MAPbBr_3$ film arrays were also achieved with the SU-8 patterns, showing a smooth surface and uniform dimensions (Figure S2a–c, Supporting Information). Two strong diffraction peaks of the

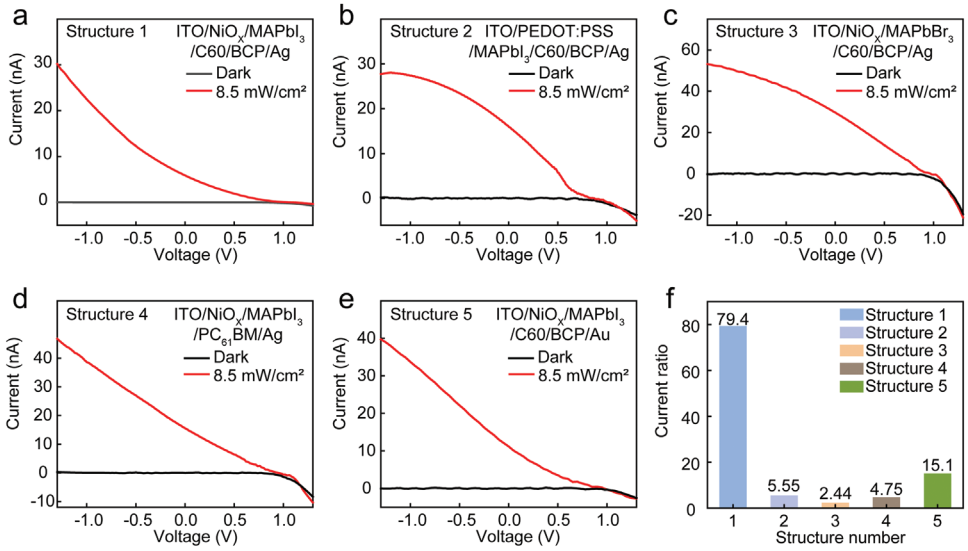


**Figure 3.** The device performance of five different self-powered photodetectors fabricated through this approach. a–e) *I–V* curves of five self-powered devices in the dark condition and under the blue light (430 nm) illumination with the intensity of 8.5 mW $cm^{-2}$. f) Current ratio of the photocurrent of these devices at -1.3 V and +1.3 V.

$MAPbBr_3$ film arrays were observed, corresponding to the (001) and (002) crystal planes of cubic $MAPbBr_3$ (Figure S2d, Supporting Information).[19] The optical properties of these perovskite film arrays were characterized using the photoluminescence (PL), time-resolved photoluminescence (TRPL) and PL mapping spectrum.[20] Both the $MAPbI_3$ and $MAPbBr_3$ perovskites exhibit no obvious change in the PL peak position and the full width at half maximum (FWHM) with the pixel dimension (Figure 2e and S2e).[21] The PL intensity demonstrates a gradual decrease, reasonably caused by the reduction in the amount of the perovskite materials. In addition, all the three $MAPbI_3$ films demonstrate an exponential decay process of the PL intensity, and their fast and slow components are of the same order of magnitude (Figure 2f).[19,22] Figure 2g and Figures S3 and S4 (Supporting Information) show the PL mapping results of the $MAPbI_3$ and $MAPbBr_3$ films arrays with different dimensions, confirming that the good uniformity of the perovskite arrays. The transmission and absorption spectrum of the bottom electrodes, HTL and perovskite films array are summarized in Figure 2h,i and Figure S2f (Supporting Information), respectively. The $MAPbI_3$ film exhibits a wide absorption range in the visible wavelength band,[23] while the absorbance of $MAPbBr_3$ film demonstrates a sharp drop at the wavelength of 520 nm,[24] which are consistent with previous reports.[25] The above results confirm that the $MAPbI_3$ and $MAPbBr_3$ films array are readily for the fabrication of high-resolution devices.

### 2.2. Fabrication of Five Types of Self-Powered Devices

This fabrication strategy is versatile and can accommodate various combinations of electrode, perovskite, ETL and HTL materials. For example, we have demonstrated five different types of self-powered devices with either $NiO_x$ or poly (3,4-ethylenedioxythiophene): poly (styrenesulfonate) (PEDOT:PSS) as the HTL, $MAPbI_3$ or $MAPbBr_3$ as the active layer, C60/BCP or [6,6]-phenyl-C61-butyric acid methyl ester ($PC_{61}BM$) as the ETL, and Ag or Au as the top electrodes, as shown in Figure S6 (Supporting Information). **Figure 3**a–e shows the typical *I–V* curves of these devices in the dark condition and under the blue light (430 nm) illumination with the intensity of 8.5 mW $cm^{-2}$. All the devices exhibit asymmetric *I–V* curves and self-powered characteristics due to the built-in electric field. The capability to block the reverse current under strong illumination is crucial for the array devices to minimize the crosstalk. Figure 3f compares the ratio of the photocurrent measured at −1.3 V and +1.3 V, respectively. The device with the structure of $ITO/NiO_x/MAPbI_3/C60/BCP/Ag$ shows the highest current ratio of 79.4. It could be explained from the band energy alignment. As shown in Figure S6 (Supporting Information),[26] electron transport from $MAPbI_3$ to $NiO_x$ requires overcoming an energy barrier of 1.6 eV,[27] while it is only 0.81 eV for the transporting to the PEDOT: PSS layer.[17] Similarly, holes must overcome a higher barrier to transport to the C60 layer compared to the $PC_{61}BM$.[28] The high barrier height reduces the reverse current, giving rise to the large current ratio. In addition, different top electrodes do not bring significantly change on the photocurrent ratio.[29] Both the Ag and Au film could be etched into high-resolution patterns, as shown in Figures S7 and S8 (Supporting Information). Considering the ease of etching, the Ag film was utilized as the top electrodes. We believe that this strategy is a universal method for fabricating the high-resolution photodetectors array based on various materials combinations.

### 2.3. Optoelectronic Performances of Devices with Different Pixel Dimensions

Comparing the crosstalk reduction capabilities of five structural devices, we choose the device with a structure of

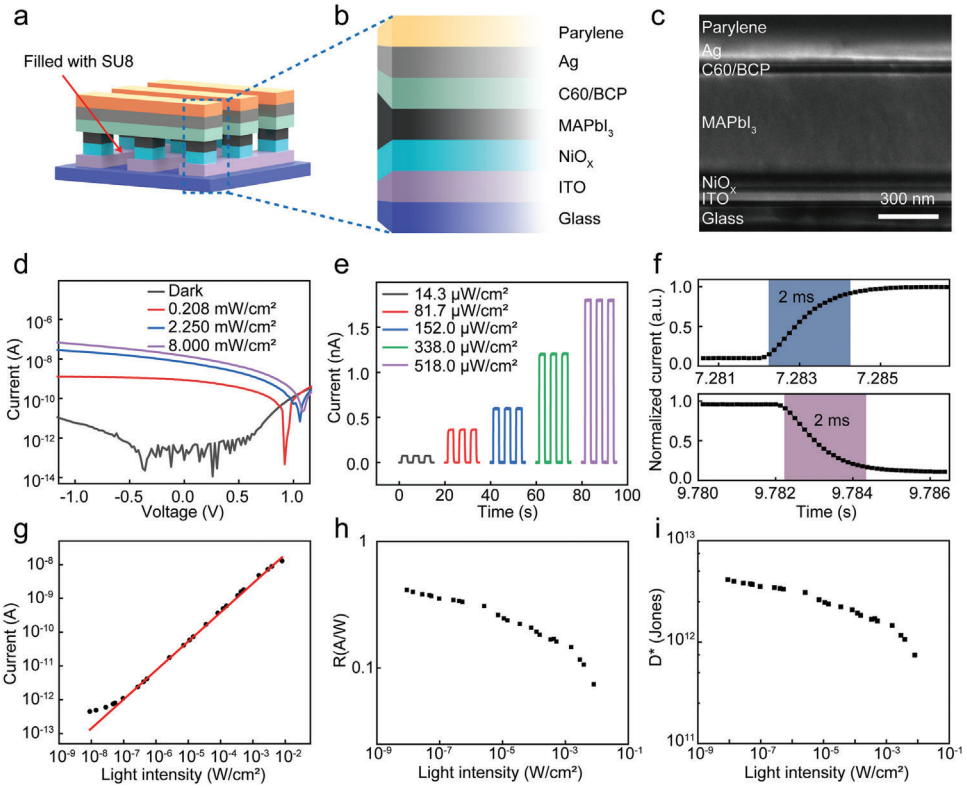


**Figure 4.** Optoelectronic performances of a high-resolution photodetectors array with the pixel dimensions of 40 μm × 40 μm. a,b) Schematic illustration of the crossbar structure of the high-resolution photodetectors array. c) Cross-sectional SEM image of the high-resolution photodetectors array. d) *I–V* curves of the device at different light intensities. e) I-t curves of the device at different light intensities with 0 V bias. f) The response and decay time under 500 nm illumination with light intensity of 8 mW $cm^{-2}$ with 0 V bias. g) Dependence of the photocurrent at 0 V bias on the light intensity. h,i) Responsivity and detectivity versus the light intensity.

ITO/$NiO_x$/$MAPbI_3$/C60/BCP/Ag to prepare array devices. The array adopted the vertical crossbar structure, consisting of 2304 pixels (48 × 48) with a resolution of 317 ppi (**Figure 4**a). Each pixel includes a $MAPbI_3$ film as the active layer, a $NiO_x$ film and C60/BCP as the HTL and ETL, respectively. The bottom electrodes are ITO stripes and easily etched Ag films serve as the top electrodes (Figure 4b). Figure 4c shows the cross-sectional SEM image of an individual pixel, where each layer is tightly stacked without gaps. Figure 4d depicts the *I–V* curves of the individual pixel of the photodetectors array with the green light illumination (500 nm) at different light intensities. The *I–V* curves exhibit rectification characteristics. Furthermore, the current at 0 V bias voltage increases significantly with the light intensity enhanced from 0 to 8 mW $cm^{-2}$, which can be attributed to strong discrete ability of the electron-hole pairs led by the built-in electric field. The current switch ratios of the devices at 0 V bias are calculated to be $3.5 \times 10^4$. The I-t curves under 0 V bias with different light intensities are plotted in Figure 4e, exhibiting stable on/off behavior at the self-powered mode. The response time and decay time were calculated using the difference between the time to reach 10% and 90% of the maximum value of the photocurrent. As shown in Figure 4f, the response time and decay time are calculated to be 2 ms and 2 ms, respectively. The self-powered photodetector arrays demonstrate the capability of the weak light detection. As shown in Figure S9 (Supporting Information), the device could resolve the weak light with an intensity of 9 nW $cm^{-2}$. Figure 4g depicts the photocurrents as a function of the light intensity of the devices, exhibiting a sublinear behavior in a wide range from 9 nW $cm^{-2}$ to 8 mW $cm^{-2}$. The photocurrent of devices can be fitted by the following equation:

$$I_{ph}=\alpha P^{\beta} \tag{1}$$

where $I_{ph}$ is photocurrent ($I_{ph} = I_{light} - I_{dark}$), $P$ is illumination intensity, $\alpha$ is a constant, $\beta$ is an exponent related to the photoresponse corresponding to the illumination power density. The best-fitting values of $\beta$ is 0.859. The responsivity and detectivity are important parameters of the photodetector. The responsivity ($R$) is defined as:

$$R=\frac{I_{light}-I_{dark}}{P \times S} \tag{2}$$

where $I_{light}$, $I_{dark}$, $P$, and $S$ are the current under illumination, dark current, illumination intensity and effective sensing area of the device, respectively. The detectivity ($D$) can be expressed as:

$$D=\frac{R}{\sqrt{2 \times q \times J_{dark}}} \tag{3}$$

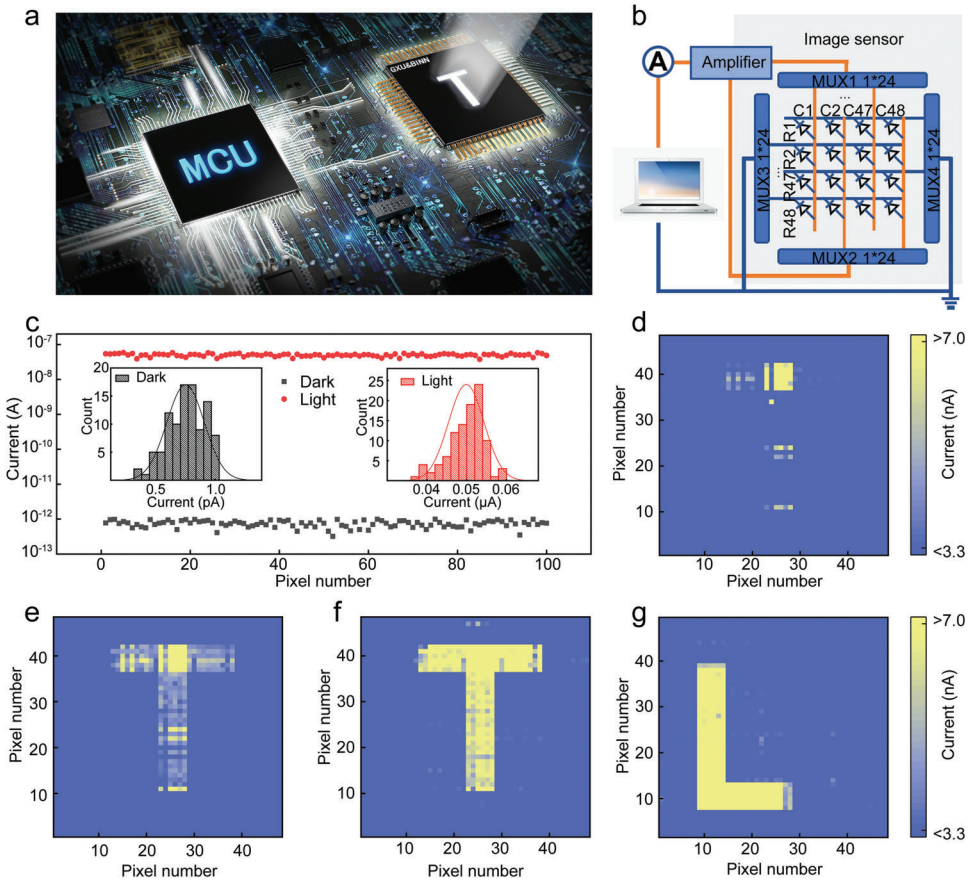


**Figure 5.** Demonstration of the imaging capability of the high-resolution photodetectors array. a) Schematic illustration of the high-resolution device integrated with the chips, circuits, and systems. b) Circuit schematic of multi-channel data acquisition system and high-resolution photodetectors array. c) Photocurrent and dark current of 100 randomly selected pixels under 2 mW $cm^{-2}$ illumination. d-f) The "T"-shaped photocurrent image obtained with the illumination intensity of 0.66, 1.45, and 2 mW $cm^{-2}$, respectively. g) The "L"-shaped photocurrent image obtained with the illumination intensity of 2 mW $cm^{-2}$.

where $q$ is the elementary charge and $J_{dark}$ is the dark current density. The responsivity and detectivity at different light intensities are shown in Figure 4h,i. At 0 V bias, the maximum responsivities of the device are 0.35 A $W^{-1}$, and the detectivity is calculated to be $5.17 \times 10^{12}$ Jones. In addition, at 0 V bias, the photodetector array exhibited a stable dynamitic switching behavior (Figure S10, Supporting Information). It maintained over 90.6% of the initial photocurrent after the long-term switching characterization for 12.8 h. As a comparison, a photodetector array with large pixel dimension of 90 μm × 90 μm was fabricated, corresponding to the resolution of 127 ppi. As shown in Figure S11 (Supporting Information), this device demonstrates the enhanced photocurrent due to the increasing of the area of the active layer, however, comparable performance with the device with 40 μm × 40 μm pixels in terms of responsivity, detectivity, response time, light detection limit and linear response range. The resolution is expected to be further improved through straightforwardly reducing the pixel dimensions of the perovskite photodiode. The comparison between our photodetectors array and other reported devices array with different structures is summarized in Table S1. Our photodetectors array demonstrates comparable performance to state-of-the-art self-powered devices in terms of responsivity and on/off ratio, and the large-scale and high-resolution features make it highly competitive for integrated systems applications.

### 2.4. Imaging Applications of High-Resolution Perovskite Photodetector Array

Finally, the imaging capability of the high-resolution perovskite photodetector array was characterized. Given its simple vertical crossbar device geometry and its fabrication process that is fully compatible with photolithography and etching techniques, the device is expected to be integrated with the chips, circuits and systems (**Figure 5**a). Here, we built a multi-channel data acquisition system for measuring of the 48 × 48 photodetectors array (Figure 5b). The 96 wires of the device were connected with this system and the output current of the selected pixel was readout by activating the shutter of the corresponding word and bit lines. To evaluate the homogeneity of the photoresponse of the pixels in the array device, we randomly selected 100 pixels and measured their output currents in the dark and under the 2 mW $cm^{-2}$ light illumination. As shown in Figure 5c, the currents under both dark and light conditions are distributed in a narrow

range. The average dark current is as low as $7.44\pm0.16 \times 10^{-13}$A, while the light current could to reach to $4.99\pm0.45 \times 10^{-8}$A, indicating a high on/off ratio of $6.70 \times 10^4$. The input light was projected onto the device array using a shadow mask. Through mapping the output current of all the pixels of the array, the input image could be reconstructed. As shown in Figure 5d–f, with increasing the light intensity, the "T"-shaped image become clearer as the light intensity increased and it could be easily recognized at the light intensity of 1.45 mW $cm^{-2}$. Moreover, as shown in Figure 5g, different patterns could also be imaged by the $48 \times 48$ photodetectors array, verifying its reliable imaging capability for various patterns and light intensities.

## 3. Conclusion

In summary, we have demonstrated a universal fabrication strategy that incorporates an ultrathin encapsulation and conventional microfabrication techniques for the high-density integration of the photodetectors. The self-powered $48 \times 48$ crossbar device with the record resolution of 317 ppi demonstrates the feasibility of this strategy, as well as its excellent photoresponse performance with high on/off ratio, capability to resolving weak light, and long-term working stability. Furthermore, the compatibility of this strategy with various material systems, combining different HTL, ETL, and perovskites in the photodiode architecture, enables its application in diverse perovskite devices. This approach has the potential to significant advance the commercialization process of perovskite arrays, especially for the large-scale, high-resolution applications.

## 4. Experimental Section

*Materials*: Indium tin oxide (ITO, 99.99%, $In_2O_3$:$SnO_2$ = 90:10 wt%), Nickel oxide (NiO, 99.9%), Ag (99.99%) and Au (99.999%) targets were purchased from ZhongNuo Advanced Material (Beijing) Technology Co., Limited. Methylammonium bromide (MABr, 99.5%), Lead bromide ($PbBr_2$, 99.99%), Fullerene (C60, 99%), 2,9-dimethyl-4,7-diphenyl-1,10-phenanthroline or bathocuproine (BCP, 99%) and Poly (3,4-ethylenedioxythiophene): poly (styrenesulfonate) (PEDOT: PSS 4083) were purchased from Xi'an Polymer Light Technology Corp. Methylammonium iodide (MAI, 99.99%), Lead Iodide ($PbI_2$, 99.999%) and [6,6]-phenyl-C61-butyric acid methyl ester ($PC_{61}BM$, 99.9%) were purchased from Advanced Election Technology CO., Ltd. 1H,1H,2H,2H-PerfluorodecyltriMethoxysilane (FAS17, 98%) was purchased from Beijing InnoChem Science & Technology Co., Ltd. N,N-Dimethylformamide (DMF, 99.9%) and Dimethyl sulfoxide (DMSO, 99.9%) were purchased from Shanghai Aladdin Biochemical Technology Co., Ltd. All of the materials were used as received.

*Characterization of Perovskite Films Array*: The surface morphologies of $MAPbI_3$ films of different sizes and cross-section of the devices were observed by scanning electron microscope (Nova NanoSEM 450). The phase analysis of perovskite films of different sizes was characterized by XRD (Xpert3 Powder). The absorption and transmittance spectrum were characterized by an ultraviolet-visible near-infrared spectrophotometer (UV3600). The PL and TRPL spectrum of different sizes of $MAPbI_3$ were characterized by a full-function fluorescence spectrometer (FLS980-S2S2-STM). The homogeneity of the PL luminescence of $MAPbI_3$ films and the PL spectrum of $MAPbBr_3$ films were characterized by confocal Raman microspectroscopy (LABRAM HR EVOLUTION).

*Characterization of High-Resolution Photodetectors Array*: To characterize the photoresponse of the photodetector, 430 and 500 nm LEDs were used as visible light sources. The *I–V* curves of the devices were characterized using the semiconductor analyzer (Keithley 4200) in dark condition and under different light intensities. The current amplifier (Stanford SR570) and function generator (Stanford DS345) were used to characterize the I-t curves and the long-term stability of the device at 0 V for different light intensities. A 500 nm parallel light source was used as the light source for imaging, and a homemade external measurement circuit with a sourcemeter (Keithley 2612B) and a system switch (Keithley 3700A) was used to test the imaging of a $48 \times 48$ imaging array.

## Supporting Information

Supporting Information is available from the Wiley Online Library or from the author.

## Acknowledgements

The authors thank the support of National Natural Science Foundation of China (No. 52125205, U20A20166, 61805015 61804011 and 52102184), Natural Science Foundation of Beijing Municipality (Z180011), Shenzhen Science and Technology Program (Grant No. KQTD20170810105439418), and the Fundamental Research Funds for the Central Universities.

## Conflict of Interest

The authors declare no conflict of interest.

## Data Availability Statement

The data that support the findings of this study are available from the corresponding author upon reasonable request.

## Keywords

high resolution, large scale, perovskite films arrays, photodetector arrays, universal fabrication strategy

Received: March 16, 2023
Revised: April 28, 2023
Published online:

[1] a) J. Zeng, L. Bi, Y. Cheng, B. Xu, A. K. Y. Jen, *Nano Res. Energy* **2022**, *1*, e9120004; b) Y. Zhao, F. Ma, Z. H. Qu, S. Q. Yu, T. Shen, H. X. Deng, X. B. Chu, X. X. Peng, Y. B. Yuan, X. W. Zhang, J. B. You, *Science* **2022**, *377*, 531. c) G. Tang, P. You, Q. Tai, A. Yang, J. Cao, F. Zheng, Z. Zhou, J. Zhao, P. K. L. Chan, F. Yan, *Adv. Mater.* **2019**, *31*, 1807689.

[2] a) Y. H. Kim, Y. X. Zhai, H. P. Lu, X. Pan, C. X. Xiao, E. A. Gaulding, S. P. Harvey, J. J. Berry, Z. V. Vardeny, J. M. Luther, M. C. Beard, *Science* **2021**, *371*, 1129; b) K. B. Lin, J. Xing, L. N. Quan, F. P. G. de Arquer, X. W. Gong, J. X. Lu, L. Q. Xie, W. J. Zhao, D. Zhang, C. Z. Yan, W. Q. Li, X. Y. Liu, Y. Lu, J. Kirman, E. H. Sargent, Q. H. Xiong, Z. H. Wei, *Nature* **2018**, *562*, 245; c) D. X. Ma, K. B. Lin, Y. T. Dong, H. Choubisa, A. H. Proppe, D. Wu, Y. K. Wang, B. Chen, P. C. Li, J. Z. Fan, F. L. Yuan, A. Johnston, Y. Liu, Y. T. Kang, Z. H. Lu, Z. H. Wei, E. H. Sargent, *Nature* **2021**, *599*, 594.

[3] a) Z. Yang, M. M. Jiang, L. J. Guo, G. F. Hu, Y. S. Gu, J. G. Xi, Z. H. Huo, F. T. Li, S. F. Wang, C. F. Pan, *Nano Energy* **2021**, *85*, 105951. b) C. Xie, C.-K. Liu, H.-L. Loi, F. Yan, *Adv. Funct. Mater.* **2020**, *30*, 1903907. c) C. Xie, P. You, Z. Liu, L. Li, F. Yan, *Light: Sci. Appl.* **2017**, *6*, e17023.

[4] J. Park, J. Kim, H. S. Yun, M. J. Paik, E. Noh, H. J. Mun, M. G. Kim, T. J. Shin, S. I. Seok, *Nature* **2023**, *616*, 724.

[5] a) C. X. Bao, W. D. Xu, J. Yang, S. Bai, P. P. Teng, Y. Yang, J. P. Wang, N. Zhao, W. J. Zhang, W. Huang, F. Gao, *Nat. Electron.* **2020**, *3*, 156; b) W. J. Cheng, W. Tian, F. R. Cao, L. Li, *InfoMat* **2022**, *4*, e12348.

[6] A. van Breemen, R. Ollearo, S. Shanmugam, B. Peeters, L. Peters, R. L. van de Ketterij, I. Katsouras, H. B. Akkerman, C. H. Frijters, F. Di Giacomo, S. Veenstra, R. Andriessen, R. A. J. Janssen, E. A. Meulenkamp, G. H. Gelinck, *Nat. Electron.* **2021**, *4*, 818.

[7] L. L. Gu, S. Poddar, Y. J. Lin, Z. H. Long, D. Q. Zhang, Q. P. Zhang, L. Shu, X. Qiu, M. Kam, A. Javey, Z. Y. Fan, *Nature* **2020**, *581*, 278.

[8] G.-H. Dun, H. Zhang, K. Qin, X. Tan, R. Zhao, M. Chen, Y. Huang, X.-S. Geng, Y.-Y. Li, Y. Li, P. Wan, G.-Y. Gou, Q.-X. Feng, X.-R. Zheng, R. Liang, D. Xie, Y. Zhou, X. Wang, H. Tian, Y. Yang, T.-L. Ren, *ACS Nano* **2022**, *16*, 10199.

[9] W. Kim, S. K. Kim, S. Jeon, J. Ahn, B. K. Jung, S. Y. Lee, C. Shin, T. Y. Seong, S. Jeong, H. S. Jang, T. N. Ng, S. J. Oh, *Adv. Funct. Mater.* **2022**, *32*, 2111409.

[10] S. Y. Liang, Y. F. Liu, S. Y. Wang, Z. K. Ji, H. Xia, B. F. Bai, H. B. Sun, *Adv. Funct. Mater.* **2022**, *32*, 0224957.

[11] L. L. Gu, M. M. Tavakoli, D. Q. Zhang, Q. P. Zhang, A. Waleed, Y. Q. Xiao, K. H. Tsui, Y. J. Lin, L. Liao, J. N. Wang, Z. Y. Fan, *Adv. Mater.* **2016**, *28*, 9713.

[12] X. P. Feng, Y. H. He, W. Qu, J. M. Song, W. T. Pan, M. R. Tan, B. Yang, H. T. Wei, *Nat. Commun.* **2022**, *13*, 6106.

[13] W. Lee, J. Lee, H. Yun, J. Kim, J. Park, C. Choi, D. C. Kim, H. Seo, H. Lee, J. W. Yu, W. B. Lee, D. H. Kim, *Adv. Mater.* **2017**, *29*, 1702902.

[14] C. Li, J. X. Li, C. Y. Li, J. Wang, X. W. Tong, Z. X. Zhang, Z. P. Yin, D. Wu, L. B. Luo, *Adv. Opt. Mater.* **2021**, *9*, 2100371.

[15] W. Q. Wu, X. Han, J. Li, X. D. Wang, Y. F. Zhang, Z. H. Huo, Q. S. Chen, X. D. Sun, Z. S. Xu, Y. W. Tan, C. F. Pan, A. L. Pan, *Adv. Mater.* **2021**, *33*, 2006006.

[16] J. Jang, Y. G. Park, E. Cha, S. Ji, H. Hwang, G. G. Kim, J. Jin, J. U. Park, *Adv. Mater.* **2021**, *33*, 2101093.

[17] Z. Y. Zhan, D. X. Lin, J. T. Cai, Y. H. Lu, A. D. Chen, T. K. Zhang, K. Chen, P. Y. Liu, X. M. Wang, W. G. Xie, *Adv. Mater.* **2022**, *34*, 2207106.

[18] B. Wang, C. Zhang, B. Zeng, C. Y. Wu, C. Xie, D. Wu, Y. X. Zhou, L. B. Luo, *J. Phys. Chem. Lett.* **2021**, *12*, 2930.

[19] J. S. Zhang, C. Li, Y. Liang, J. P. Song, Q. Y. Shang, L. Y. Zhao, H. F. Tian, L. Liu, Q. Zhang, *Adv. Funct. Mater.* **2023**, *33*, 2208841.

[20] K.-K. Liu, Q. Liu, D.-W. Yang, Y.-C. Liang, L.-Z. Sui, J.-Y. Wei, G.-W. Xue, W.-B. Zhao, X.-Y. Wu, L. Dong, C.-X. Shan, *Light Sci Appl* **2020**, *9*, 44.

[21] a) Y. Q. Wu, P. Wang, X. L. Zhu, Q. Q. Zhang, Z. Y. Wang, Y. Y. Liu, G. Z. Zou, Y. Dai, M. H. Whangbo, B. B. Huang, *Adv. Mater.* **2018**, *30*, 1704342; b) H. F. Zarick, A. Boulesbaa, A. A. Puretzky, E. M. Talbert, Z. R. DeBra, N. Soetan, D. B. Geohegan, R. Bardhan, *Nanoscale* **2017**, *9*, 1475.

[22] T. Zhao, C. C. Chueh, Q. Chen, A. Rajagopal, A. K. Y. Jen, *ACS Energy Lett.* **2016**, *1*, 757.

[23] T. Zhu, L. N. Shen, H. L. Chen, Y. R. Yang, L. Y. Zheng, R. Chen, J. Zheng, J. P. Wang, X. Gong, *J. Mater. Chem. A* **2021**, *9*, 21910.

[24] A. Ishteev, K. Konstantinova, G. Ermolaev, D. Kiselev, D. S. Muratov, M. Voronova, T. Ilina, P. Lagov, O. Uvarov, Y. Pavlov, M. Letovaltseva, A. Arsenin, V. Volkov, S. Didenko, D. Saranin, A. Di Carlo, *J. Mater. Chem. C* **2022**, *10*, 5821.

[25] Z. Y. Zhang, H. Y. Wang, Y. X. Zhang, Y. W. Hao, C. Sun, Y. Zhang, B. R. Gao, Q. D. Chen, H. B. Sun, *Sci. Rep.* **2016**, *6*, 27286.

[26] a) J. Chakrabartty, M. A. Islam, S. Reza, *Sol. Energy* **2021**, *230*, 195; b) S. Y. Guo, S. Qiao, J. H. Liu, J. K. Ma, S. F. Wang, *Opt. Express* **2022**, *30*, 11536; c) Y. C. Hu, Z. Q. Yang, X. Cui, P. Zeng, F. M. Li, X. C. Liu, G. Q. Feng, M. Z. Liu, *ACS Appl. Mater. Interfaces* **2022**, *14*, 13431; d) M. B. Islam, M. Yanagida, Y. Shirai, Y. Nabetani, K. Miyano, *ACS Omega* **2017**, *2*, 2291; e) G. X. Li, Y. K. Wang, L. X. Huang, W. H. Sun, *J. Alloy. Compd.* **2022**, *907*, 164432.

[27] A. M. Afzal, I. G. Bae, Y. Aggarwal, J. Park, H. R. Jeong, E. H.a Choi, B. Park, *Sci. Rep.* **2021**, 11.

[28] a) Y. Gao, W. Z. Xu, F. He, P. B. Nie, Q. D. Yang, Z. C. Si, H. Meng, G. D. Wei, *Nano Res.* **2021**, *14*, 2294; b) Y. Zhang, Z. L. Qin, W. Q. Nie, Y. Q. Li, X. M. Huo, D. D. Song, B. Qiao, Z. Xu, S. Wageh, A. Al-Ghamdi, S. L. Zhao, *Adv. Opt. Mater.* **2022**, *10*, 2200648.

[29] Z. B. Li, H. A. Li, K. Jiang, D. Ding, J. N. Li, C. Ma, S. C. Jiang, Y. Wang, T. D. Anthopoulos, Y. M. Shi, *ACS Appl. Mater. Interfaces* **2019**, *11*, 40204.